Optical Engineering

OpticalEngineering.SPIEDigitalLibrary.org

Detector with internal gain for short-wave infrared ranging applications

Vala Fathipour
Hooman Mohseni

SPIE.

Vala Fathipour, Hooman Mohseni, "Detector with internal gain for short-wave infrared ranging applications," *Opt. Eng.* **56**(9), 091608 (2017), doi: 10.1117/1.OE.56.9.091608.

Detector with internal gain for short-wave infrared ranging applications

Vala Fathipour and Hooman Mohseni*
Northwestern University, Bio-Inspired Sensors and Optoelectronics Laboratory, Evanston, Illinois, United States

Abstarct. Highly sensitive photon detectors are regarded as the key enabling elements in many applications. Due to the low photon energy at the short-wave infrared (SWIR), photon detection and imaging at this band are very challenging. As such, many efforts in photon detector research are directed toward improving the performance of the photon detectors operating in this wavelength range. To solve these problems, we have developed an electron-injection (EI) technique. The significance of this detection mechanism is that it can provide both high efficiency and high sensitivity at room temperature, a condition that is very difficult to achieve in conventional SWIR detectors. An EI detector offers an overall system-level sensitivity enhancement due to a feedback stabilized internal avalanche-free gain. Devices exhibit an excess noise of unity, operate in linear mode, require bias voltage of a few volts, and have a cutoff wavelength of 1700 nm. We review the material system, operating principle, and development of EI detectors. The shortcomings of the first-generation devices were addressed in the second-generation detectors. Measurement on second-generation devices showed a high-speed response of ~6 ns rise time, low jitter of less than 20 ps, high amplification of more than 2000 (at optical power levels larger than a few nW), unity excess noise factor, and low leakage current (amplified dark current ~10 nA at a bias voltage of −3 V and at room temperature. These characteristics make EI detectors a good candidate for high-resolution flash light detection and ranging (LiDAR) applications with millimeter scale depth resolution at longer ranges compared with conventional p-i-n diodes. Based on our experimentally measured device characteristics, we compare the performance of the EI detector with commercially available linear mode InGaAs avalanche photodiode (APD) as well as a p-i-n diode using a theoretical model. Flash LiDAR images obtained by our model show that the EI detector array achieves better resolution with higher signal-to-noise compared with both the InGaAs APD and the p-i-n array (of 100 × 100 elements). We have designed a laboratory setup with a receiver optics aperture diameter of 3 mm that allows an EI detector (with 30-μm absorber diameter) to be used for long-range LiDAR imaging with subcentimeter resolution.
[DOI: 10.1117/1.OE.56.9.091608]

Keywords: photodetector; infrared imaging; infrared detector; electron-injection detector; phototransistor.

Paper 161631SSP received Oct. 19, 2016; accepted for publication Feb. 13, 2017; published online Mar. 22, 2017.

1 Introduction

A photon is defined as a fundamental excitation of a single mode of the quantized electromagnetic field.[1] Planck was the first person to explain the blackbody radiation spectrum in 1900. He explained this behavior by quantization of electromagnetic radiation. Einstein utilized this concept to explain the photoelectric effect[2] in 1905, and Compton used it to explain the wavelength shift of scattered x-rays in 1923. Lewis introduced the term "photon" for the first time in 1926.[2,3] The formal quantization of the electromagnetic field was first introduced by Dirac in 1927.[2] A single photon in mode k has energy equal to $h\nu$k, where h is the Planck's constant and νk is its frequency.[2]

The photon can be detected by a solid-state detector if it can generate mobile charges (signal quanta) in the detector material. Single-photon imaging for high-energy photons (ultraviolet or x-ray) has existed for many years. It started as early as ~1912 using "cloud chamber," which is an "imaging detector,"[4–6] and switched to using solid-state electronic detectors in the 1970s (Fig. 1). Today, solid-state high-energy photon detectors excel technologically, and large area (~m^2) detectors are being built for the large hadron collider (LHC)-collider.[14–18] Imaging in ultraviolet or x-ray region is easy to accomplish as the large photon energy is converted into a number of charged pairs,[12] which represent the photon energy.[19] Despite the fact that single-photon detection and imaging for longer wavelengths have also existed for many years, they have until now developed very slowly.[20,21] This is because detection of longer wavelengths requires utilization of semiconductors with a smaller energy bandgap (Eg) for the creation of the mobile charges, as shown in Eq. (1):

$$E\mathrm{g} = hc/\lambda\mathrm{g}, \tag{1}$$

where λg is the cutoff wavelength, h is the Planck's constant, and c is the speed of light. Reduction of Eg, however, results in the exponential increase of the generation recombination dark current density of the detector (J_{GR}); as such, semiconductor detectors have relatively poor performance at longer wavelengths. This is shown as

$$J_{\mathrm{GR}} \alpha T^{3/2} e^{-\mathrm{Eg}/2KT} W(V), \tag{2}$$

*Address all correspondence to: Hooman Mohseni, E-mail: hmohseni@northwestern.edu

0091-3286/2017/$25.00 © 2017 SPIE

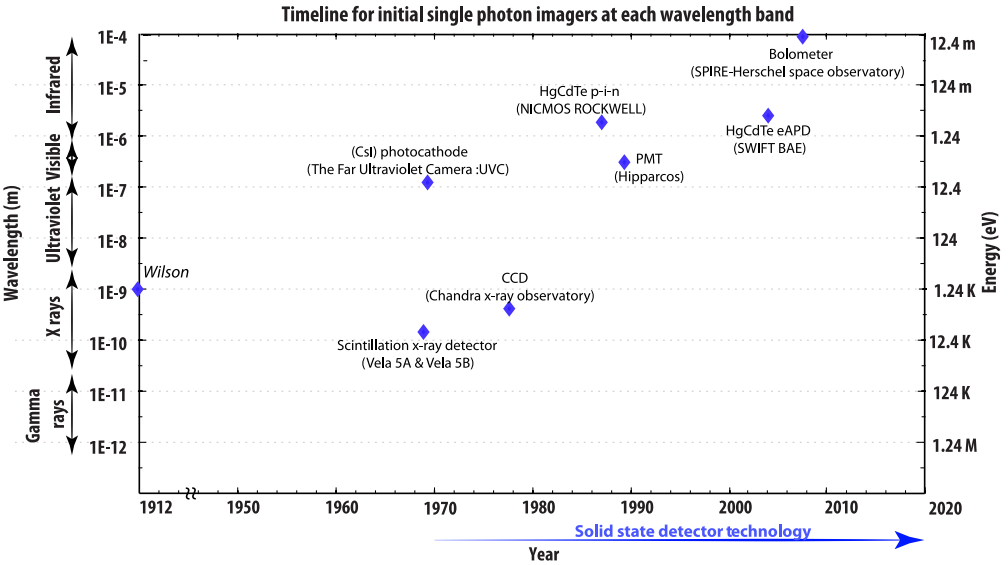

Fig. 1 Timeline of initial demonstrations of single-photon imager instrumentation. The cutoff wavelength for each technology is shown by markers. The general trend that x-ray imagers with single-photon sensitivity were demonstrated first, then visible, and then infrared shows the importance and the challenge of imaging at the single-photon level at lower photon energy levels. Today, single-photon image sensors operating at visible wavelength are increasingly available even to the consumer market. Data obtained from Refs. 7–13.

where T is the temperature and W is the depletion width, which is a function of applied bias voltage, V. From Eq. (2), it can be concluded that single-photon detection is severely hampered at the infrared regime, and room-temperature single-photon electronic imaging is restricted to detector materials with λ_g below about 1.3 μm.[19]

Another chronic difficulty especially for visible and infrared photon-starved imaging conditions, such as in low light surveillance imaging[7] through high-speed, single-photon imaging for the life sciences[8,9] and in astronomical observations, is the readout noise. This is the additional noise added by the electronic charge detection circuit, where the detected photoelectrons are converted into an output voltage or current signal. The readout noise becomes more severe when high frame rate imaging is required. Detectors without any internal amplification, such as the charged-couple devices (CCDs), which is the first widely commercialized electronic imaging technology,[10] and the p-i-n diodes, are inherently unable to provide accurate measurements of fast low-intensity transients at high frame rates. In fact, the ultimate sensitivity limitation of a CCD or a p-i-n detector is set by the readout noise of the first-stage amplifier, which becomes more severe at faster readout rates.[11] To be able to respond to single photons, the photon detector must exploit an internal multiplication process to achieve subelectron input referred readout noise.[12] Although the noise contribution of such detectors is unavoidable and is always higher than a p–i–n diode, the contribution from the amplifier can be lower than the detector in the presence of gain in the detector.[13,22] Detectors with an internal amplification of the charge carriers are suitable for high frame rate single-photon imaging including photomultipliers (PMTs), avalanche photodiodes (APDs), and electron-multiplying CCDs (EMCCDs).

While visible PMTs are impressive as a pioneering technology, they cannot satisfy requirements of many modern applications as they rely on vacuum tube technology. This prevents their ability to be assembled in large arrays with high pixel density. Furthermore, for infrared region, PMT performance is poor compared with the visible wavelength.

Solid-state CCDs utilizing electron multiplication (EMCCDs) became commercially available in 2001.[23,24] Similar to CCDs, EMCCDs are inherently suited for imaging applications, while providing enhanced signal-to-noise ratio (SNR) for signal levels below the CCD readout noise floor. This is achieved in the EMCCD by increasing the signal through impact ionization. However, they exhibit an inherent uncertainty in the multiplication process, which elevates their noise levels, and they present an excess noise factor $F^2 \sim 2.2$.[25,26] Furthermore, due to their readout technique, they cannot be utilized in high frame rate imaging.[7,27] The highest data rates presented within this technology are operations up to a clock frequency of 35 MHz.[28] Extremely fast imaging can be performed with image intensified CCDs (ICCDs).[29] However, ICCDs are not a fully solid-state technology. As such, ICCDs are not a creditable alternative to EMCCDs in high frame rate imaging applications. Finally, EMCCDs have a wavelength sensitivity of ~0.3 to ~1.1 μm and are not suitable for infrared imaging.

The APD, developed in the 1960s, uses a similar process to the PMT but in a semiconductor platform.[30,31] APD detector arrays satisfy the significantly increased demands on high pixel rates, and frame rates as high as 1 GHz have been reported in the literature.[32] Unfortunately, APDs require high bias voltages and are sensitive to material inhomogeneity. As such, to benefit from their advantages in focal plane arrays (FPAs), specifically designed readout circuits capable of applying a high bias with very low noise are critical. Furthermore, due to a superexponential gain characteristic, the yield in achieving uniform arrays is low. For example, a mere fraction of a percent variation in the epilayer

thickness or doping concentration results in sizeable shifts in the APD output voltage that may render an array unusable.[33] The large electric field in the device leads to surface breakdown mechanisms, and consequently guard rings are required to prevent this phenomenon. The guard rings increase the pixel pitch and reduce the fill factor. Furthermore, the APD pixels need to be spaced apart to prevent cross talk due to carrier re-emission. Hence, realization of high-resolution imagers has remained a challenging task for APD-based imagers. Recent advances in device design and epitaxial growth have made the formation of 256×320 pixel arrays with 30-μm pitch possible.[34,35] On the other hand, detector technologies with a lower electric field and with stable characteristics, such as p-i-n detectors, are less sensitive to material inhomogeneities. As such, they can form high-density large-area imaging FPAs with array sizes growing in proportion to the ability of readout circuit technology to read, process, and demonstrate the detector signals. For example, currently, p–i–n-based FPAs with 4096×4096 pixel arrays and 10-μm pixel pitch are available (Hawaii-4RG).[36–38] Unfortunately, short-wave infrared (SWIR) APDs based on III-V material exhibit typical noise factors of $F \sim 4$ to 5,[39] which is caused by the stochastic nature of the gain process.[40,41] As such, a huge amount of work to reduce the multiplication noise in APDs has been reported in the literature.[42–44] The mercury cadmium telluride (HgCdTe) material system has addressed this issue, and for the midwave infrared (MWIR) and long-wave infrared spectral ranges, detectors have an excess noise factor of near-unity.[45–47] This is the result of a nearly exclusive impaction ionization of the electrons.[39] Unfortunately, in the SWIR region between 1 and 2.5 μm, which has vast applications including telecommunication, remote sensing, astronomical observation, spectro-radiometry, and spectro-photometry, the HgCdTe "electron-initiated APDs (eAPDs)" do not offer any gain.[48] For the SWIR region, to obtain gain with a near-unity excess noise, detectors with a bandgap in MWIR are typically cooled to ~60 K.[49,50] The extensive cooling is because HgCdTe eAPDs utilize a bandgap that is much smaller than what is needed for SWIR detection. Furthermore, low-pass filters are utilized to filter out the longer wavelengths.[51]

Electron-injection (EI) detectors are an alternative approach to above detection technologies and were introduced in 2007.[52] They utilize the exact bandgap required for SWIR detection and have a cutoff wavelength of 1700 nm. Compared with the SWIR HgCdTe eAPDs, they require much less cooling. Similar to p-i-n diodes, they operate at CMOS compatible bias voltages[53] and have a low electric field in the device (~40 KV/cm). This technology, together with the stable detector characteristics, makes formation of large-format high-pixel-density FPAs less challenging for low photon flux applications. Similar to linear mode APDs and EMCCDs, they provide an internal amplification, which suppresses the readout noise. On the other hand, unlike APDs and EMCCDs, due to an inherent negative feedback inside the device, the amplification mechanism is avalanche-free and stable, and the devices show an excess noise of near-unity.[54–57] Another benefit of this technology is that it satisfies the significantly increased demands on pixel rates (micro/nanosecond level acquisition times is possible) as a result of its large stable gain and high-speed response.[58] Another advantage for EI detectors over HgCdTe eAPDs is that they are based on the mature InP material system and are realized by virtue of the widely available commercial III-V-based foundries.

2 Layer Structure and Band Diagram

EI device schematic is shown in Fig. 2(a). The layer structure consists of 1000 nm n^--doped $In_{0.53}Ga_{0.47}As$ absorber, 50 nm p^+-doped $GaAs_{0.52}Sb_{0.48}$ trapping layer, 50 nm-undoped $In_{0.52}Al_{0.48}As$ etch stop, 500 nm n^+-doped InP injector, and 50 nm n^+-doped $In_{0.53}Ga_{0.47}As$ capping layer. The epitaxial layers are grown with metal organic chemical vapor deposition on 2-in. InP substrates. The band diagram through the central axis of the device as a function of depth, in darkness (blue) and under illumination (red), is shown in Fig. 2(b). When an electron–hole pair is generated in an InGaAs absorber through optical excitation, the hole is trapped in a very small volume (GaAsSb trapping layer). This creates a high concentration that reduces the potential barrier and leads to the injection of many electrons to the absorption layer.[52,59]

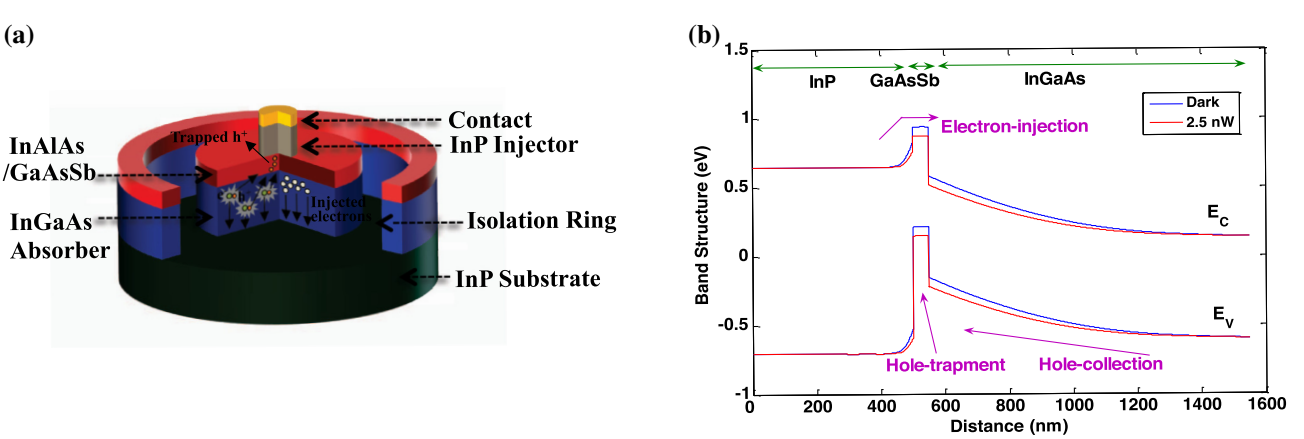

Fig. 2 (a) The schematic diagram with a cross section showing the layer structure and (b) the band diagram through the central axis as a function of depth: in darkness (blue) and under illumination (red) for an EI detector.

3 Background on Electron-Injection Detector

First EI imager with 320×256 pixel array and 30-μm pixel pitch was demonstrated in 2010 using off-the-shelf CMOS readout circuit with 575 to 870 electrons rms noise.[57,60,61] As a result of the internal charge amplification mechanism in the detector, the measured imager noise was reduced to 28 electrons rms at a frame rate of 1950 frames/s. These devices were slow (a few KHz bandwidth) and had large dark currents ($\sim$6 μA at -1.5 V, which prevented long integration times in the camera. The shortcomings of the first-generation devices were addressed in the second-generation detectors. Compared with first-generation detectors, the second-generation devices achieved 2 orders of magnitude lower dark current and 4 orders of magnitude enhancement in bandwidth. Compared with the best-reported linear mode avalanche photo detector (SWIR HgCdTe), the second-generation EI detector shows over 2 orders of magnitude lower dark current density at all measured temperatures.[54]

Second-generation devices achieved high gain ($\sim$2000), high bandwidth (fast rise time of $\sim$10 ns at 20 μW of optical power), unity excess noise factor, and low leakage current (internal dark current density of $\sim$1 μA/cm^2 at RT decreasing to 1 nA/cm^2 at 210 K) at bias voltage of -3 V. A performance comparison with other SWIR detector technologies with internal amplification showed improved performance in terms of noise-equivalent sensitivity with existing SWIR detectors, such as APDs.[56] In the EI detectors, the optical gain dropped from $\sim$2000 to $\sim$30 across an input power of 10 to 1 nanowatt.[62] The origin of the drop in optical gain at low optical powers is related to the recombination current in the injector/trapping layer heterojunction and has been extensively discussed in our publications.[58,62] Recently, we have reduced defects at heterojunction and verified the above statement with our devices that have a gain of $\sim$1000 even at very low photon flux.

These improvements have opened up applications for these detectors in the medical field [optical coherence tomography (OCT)],[63] remote sensing [light detection and ranging (LiDAR)],[64] and astronomy (exoplanet detection). In Sec. 4, we elaborate on the application of EI devices in LiDAR.

4 Utilization of Electron-Injection Detectors in Light Detection and Ranging

Most of the modern imaging techniques can only image the two-dimensional projection of a scene and loose the depth information. However, our everyday lives involve three-dimensional (3-D) views, which is much more beneficial in apprehending the characteristics of the targets. 3-D imaging has attracted increasing attentions especially in the field of biology, medical settings, industrial, and consumer applications.[65,66] Holography, which was demonstrated after the invention of the laser, is one of the longest established 3-D imaging techniques. OCT, discussed in Ref. 63, is another emerging technology for noninvasive imaging; it is based on the principle of interferometry of light waves performing high-resolution 3-D imaging deep into the tissue. LiDAR is yet another 3-D imaging and spatial measurement technique that is an integral part of any autonomous vehicle or robot and is becoming ubiquitous in many disciplines. In this approach, spatial coordinates associated with each pixel are recorded in a range image acquired by the detector. To obtain the range image, the return time of laser pulses reflected from a target is measured. By steering the transmitted light, many different points of an environment can be measured to create a full 3-D model. LiDAR has proven to be a vital technology for a variety of applications, including autonomous vehicles, automated process control, target recognition, robots, collision avoidance, remote sensing, aerial surveying, power grid facilities, architectural and structuring mapping, and oceanographic and archaeological detection. Due to its numerous applications in urban areas, SWIR is the wavelength of choice for a LiDAR system. Operating in SWIR (1.5 to 1.8 μm) would allow the maximum eye-safe power to be at least 100 times higher than the visible wavelength.

Despite the extreme usefulness and applications of LiDAR systems today, they are not on every site. This mainly stems from their bulkiness, high cost, and slow speed of operation. Furthermore, today's systems lack millimeter scale resolution at longer ranges. Among the different components of a LiDAR receiver system, the optical detector directly affects the instrument sensitivity performance. Current detector technologies for SWIR LiDAR systems are InGaAs p-i-n detectors,[67] InGaAs APDs,[68,69] or HgCdTe eAPDs.[70]

p-i-n detectors can offer extremely good range resolution as a result of their high-speed response and good timing resolution (transit time limited jitter). Jitter values $\sim$15 ps have been reported in small area devices (15-μm diameter).[71] However, these detectors are typically utilized in short-range LiDAR systems[67,72] and require high-power lasers to be able to obtain long-range imaging. The Army Research Lab (ARL) reported the development of a compact short-range LiDAR system that utilized four 1-mm-diameter InGaAs p-i-n detectors on the receiver. The transmitter used a tunable 200 to 400 kHz, 2.6-ns pulse width, and 1.5-μm laser with peak power of 1 KW. At 20 m, their system obtained 40-cm range resolution and had 256 (h) $\times$ 128 (v) pixels. To increase the range, their future work included modifying their receiver using APD-based detectors instead of p-i-n detectors. Using the APD-based receiver design, they expected to be able to image targets with a reflectivity of 0.1 at a 50-m range.

LiDARs based on APDs operate at lower power levels or longer ranges. Unfortunately, InGaAs APDs have an extra noise mechanism compared with p-i-n photodiodes (the so-called excess noise). The high excess noise factor and the low gain prevent them from achieving their ideal shot-noise limited SNR performance when operated in linear mode. As such, they are usually operated in the Geiger mode for LiDAR applications. The advantage to this mode of operation in a flash LiDAR is that variations in the gain from pixel to pixel or as a function of operating parameters or just due to statistical variations become irrelevant. Furthermore, to maintain an acceptable noise, InGaAs APDs have to be gated. These nonlinear effects severely limit the applications of InGaAs APDs in LiDAR, where the signal dynamic range spans 2 to 3 orders of magnitude and the signal arrival time is difficult to predict. Finally, APDs have a non-Gaussian probability distribution of jitter. The InGaAs/InP APDs have jitter values of about 60 ps with single photons,[73,74] and researchers have reported achieving 30 ps with some trade-offs.[75] The MIT Lincoln Laboratory

reported a LiDAR system that utilized 4×4 InGaAs Geiger-mode APD arrays, where each detector was 400 μm. Using a 1-kHz, 30-μJ micro-Nd:YAG laser at 1 μm, they obtained a 75-cm range resolution at a range of 58 m by averaging 200 frames LiDAR images.[76] As mentioned in Sec. 1, APDs based on HgCdTe have addressed this challenge and offer unity excess noise factor.[45,49,48] However, for SWIR region, detectors with a bandgap in MWIR are typically cooled to 60 K.[50,77] As well as the cooling requirement, unfortunately, the need for high bias voltages and the low yield in achieving uniform arrays makes formation of large area high-resolution flash LiDAR systems a challenging task for APD-based imagers. LETI/SOFADIR used a 320×256 HgCdTe eAPD array with a laser at 1.57 μm, pulse width of 8 ns, and pulse energy of 8 mJ. They obtained a ranging resolution of about 15 cm at a range of 30 m. For this result, the detector had avalanche gain of 23 and was cooled to 80 K.[70] Table 1 compares the obtained range, resolution, detector temperature, and peak laser power used in each of the above LiDAR systems.

Here, we utilize EI detector technology for high-resolution, long-range LiDAR systems. As mentioned in Sec. 1, similar to p-i-n diodes, the EI detectors operate at CMOS compatible bias voltages[78] and have low noise and low leakage current. The jitter in electron-injector detectors is also transit time limited and detectors achieve (extremely good) approximately tens of picoseconds of jitter performance.[58] The low electric field in the device together with a sublinear gain dependence on the bias voltage makes the formation of high yield, large-format high pixel density FPAs less challenging with this technology for low photon flux flash LiDAR applications.[38,59] Here, by providing images based on detailed theoretical modeling using experimentally measured detector data, we show that EI detectors enhance LiDAR's resolution and sensitivity. We have validated these results by comparing the LiDAR backscatter profiles obtained from the EI detector and commercial InGaAs p–i–n and APD detectors from Hamamatsu theoretically. We then demonstrate our initial laboratory setup for obtaining preliminary experimental results, which utilizes a small area detector (diameter of 30 μm).

Detector gain, rise time, and jitter were measured at different optical power levels, and the results are shown in Fig. 3.

Verification of LiDAR sensitivity enhancement: Based on the measured detector characteristics, a model was developed in Python to validate the expected performance improvement for EI detectors in a LiDAR system. Our model assumes a 1550-nm source laser, with a spectral width of 0.01 nm, divergence of 1 mrad, beam diameter of 1 cm, laser transmitter efficiency of 0.9, and 6 mJ of energy. The receiver diameter is 10 cm, with a field of view (FOV) of 40 mrad (full cone angle). The power returned to the device was calculated by assuming that the target was an ideal Lambertian surface with an albedo of 0.35 at 0.2 km. Figure 4 compares EI detector responses in this system for two cases of single pulse and 100 shot averages. Flash LiDAR images, assuming 100×100 pixels, are demonstrated in Fig. 4(a) with no averaging and in Fig. 4(b) with 100 times averaging. Cross-section profiles along the middle row of single shot image and 100 shot images are provided in Figs. 4(c) and 4(d), respectively. For this calculation, a simple square target (of reflectivity 0.35) was assumed with a perimeter background whose reflectivity is half that of the target, just to show some contrast. The power was assumed to be spread out uniformly over the whole format.

Figure 5 shows the pulse-response comparison of results provided by the EI detector (a), Hamamatsu G8931-20 APD, and the Hamamatsu 11193 p-i-n averaged over 100 shots.

Figure 6 shows the images obtained with cameras with EI detector array, APD array, and p-i-n array. Here, we assumed 100×100 imaging arrays of each detector technology: (a) shows EI detector, (b) shows Hamamatsu G8931-20 APD, and (c) shows Hamamatsu 11193 p-i-n array. For this plot, data are averaged over 100 shots.

Laboratory setup design: Here, we demonstrate an experimental measurement setup that would allow the utilization of a second-generation EI detector in a LiDAR

Table 1 Performance comparison of EI detector array with the existing SWIR LiDAR detectors.

	Detector type	Range (m)	Resolution (cm)	Pulsed laser peak energy	λ (μm)	Receiver optics	System size	T (K)
ARL[72]	Four InGaAs p-i-n detectors (1-mm-diameter detector)	20	40 measured	~2.6 μJ, 2.6 ns, 200 kHz, fiber laser	1.5	Tapered fiber bundle	Fitted on iRobot PackBot	300
MIT[76]	4×4 InGaAs Geiger-mode APD (400-μm detector)	58	75 measured	1 kHz, 30 μJ, micro-Nd:YAG laser	1.0	10-cm parabolic/pair telescope, reimaged into Maksutov telescope	13×21 in. box	300
LETI/SOFADIR[70]	256×320 pixels and 30-μm pitch eAPD array	30	15 measured	8 mJ, 8 ns	1.5	Telescope	Optical table mounted	80
NU	EI detector (320×256 pixels and $30 - \mu m$ pitch)	200	0.3 (calculated based on measured detector jitter)	40 ns, 6 mJ pulses fiber laser	1.5	3-mm MEMS mirror	Can fit on iRobot PackBot	300

Note: T denotes the temperature, λ denotes the wavelength, ARL denotes the Army Research Lab, MIT denotes the MIT Lincoln Laboratory, and NU denotes Northwestern University.

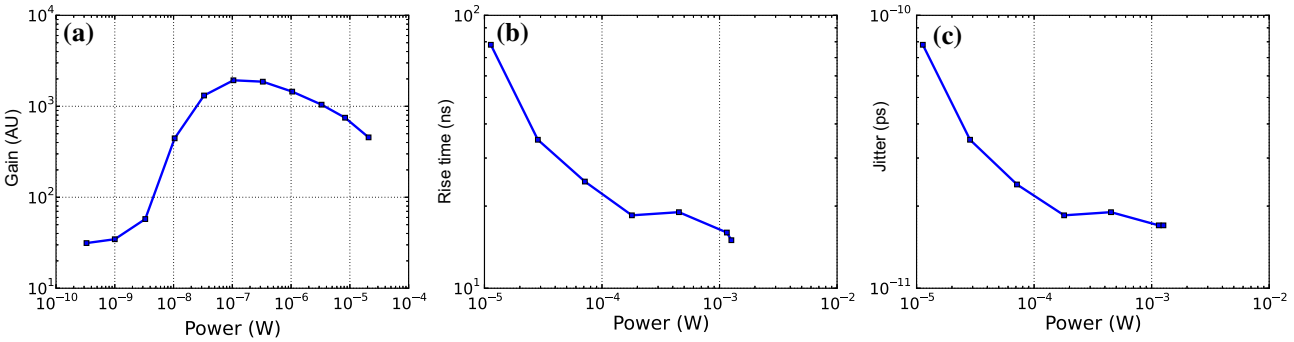

Fig. 3 Second-generation EI detector characteristic at various optical power levels: (a) gain, (b) rise time, and (c) jitter.

system, despite its extremely small (30 μm) active area. Such a system could then be transformed into the first flash LiDAR based on EI detectors with a better sensitivity than the reported performance. In a typical LiDAR system, while the transmitted beam is scanned over the scene, the receiver should see the entire scene.[72] In this approach, the detector not only picks up a large background noise but also has to be large. Detectors larger than approximately a few millimeters are typically used to maintain the required FOV. The large area of the detector increases the detector resistance capacitance time constant and degrades jitter performance. An InGaAs p-i-n detector with a 1-mm area has a transit time

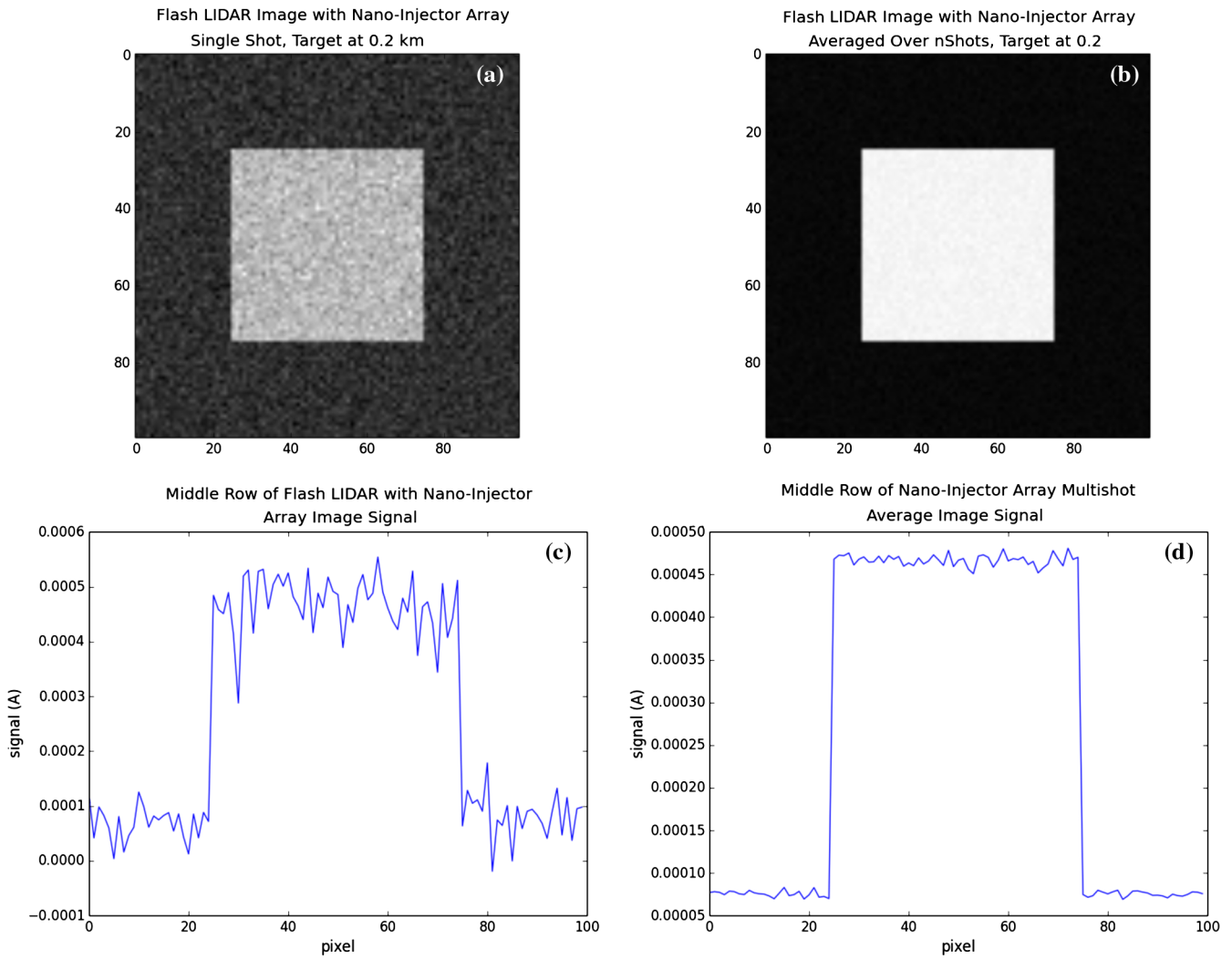

Fig. 4 To assess the performance of the second-generation electron-injector detector in a LiDAR system, a model was developed in Python based on measured experimental data. EI detector responses are presented here: (a) flash LiDAR image single pulse and (b) flash LiDAR image 100 shot averages. The cross-section profile along the middle row of image: (c) single shot and (d) 100 shot.

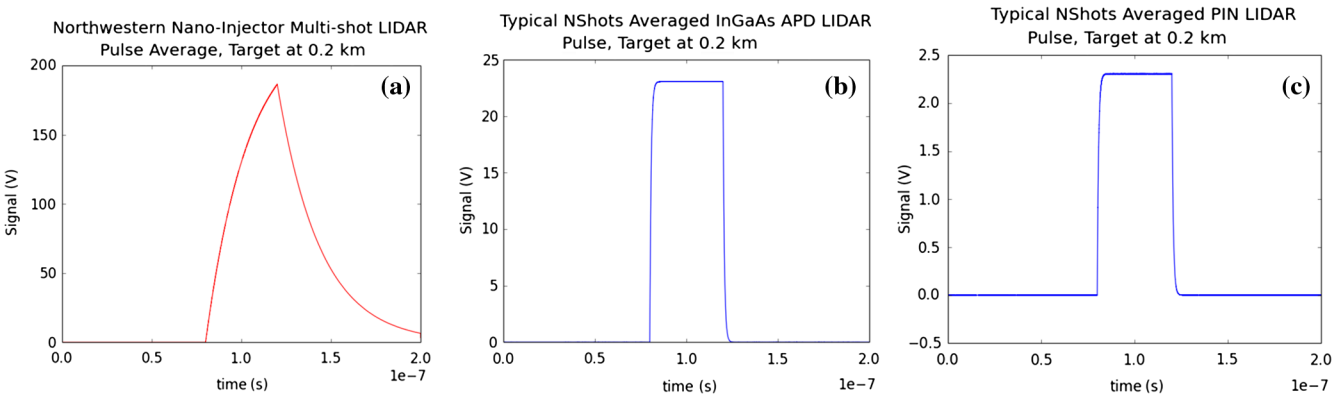

Fig. 5 Typical LiDAR 100 shot pulse average target at 0.2 km: (a) EI detector, (b) APD detector, and (c) pin detector.

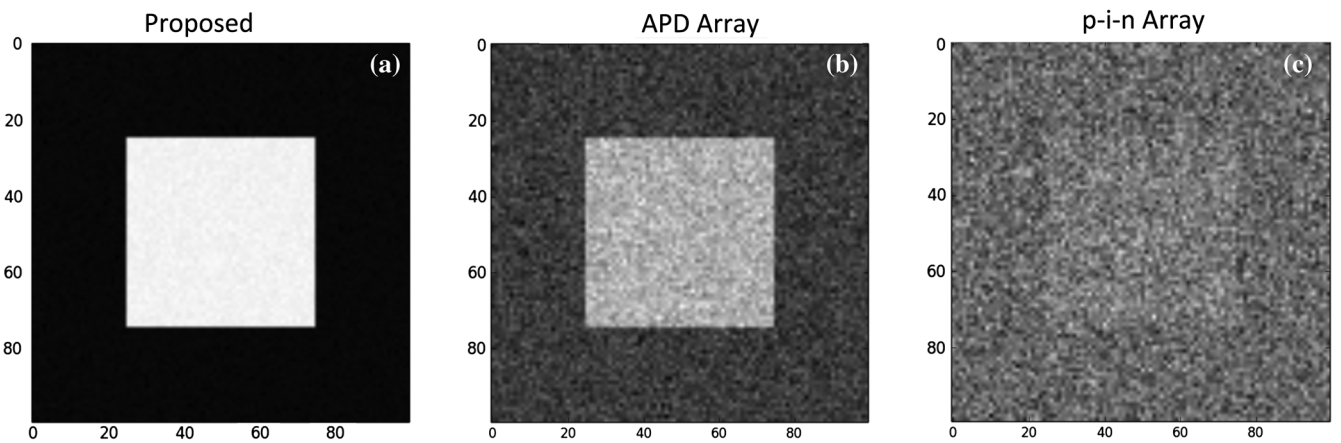

Fig. 6 Flash LiDAR images using 100×100 arrays with (a) EI detectors, (b) APD detectors, and (c) pin detectors, using 100 shot averages.

limited jitter of approximately a few nanoseconds (assuming a saturation velocity of $\sim 6 \times 10^7$ cm/s[79]). This results in ~40-cm depth resolution.[70] To eliminate the need for a large detector, one could use an extremely large numerical aperture (much larger than 1), which is not practical.

In our approach, the detector has a small FOV. The FOV is, however, scanned actively together with the laser beam. The detector remains on axis and is not scanned. The system block diagram is shown in Fig. 7. In our setup, the beam is coupled into the instrument using a beam splitter and is scanned on the scene by the MEMS mirror. The same MEMS collects light from scene and sends it to detector. The system achieves 4-mm axial resolution, 3-mm depth resolution, and 303×303 pixels (limited by the number of resolvable points on the mirror) at ~15-m range with an eye safe laser. The laser source has a central wavelength of 1550 nm, with an average power of 8 W and 40-ns pulse width. The pulse repetition frequency is variable between 100 kHz (80 μJ) and 1000 kHz (8 μJ), and the laser is linearly polarized with 15 dB PER and has 15% ASE. The laser is fiber coupled with an NA < 0.08. As such, we utilize a beam expander (collimator) that can work with the given low NA fiber and produce the beam diameter of 3 mm, which is dictated by our MEMS mirror size and is the size of our receiving aperture. All components in our setup are rated for the average and peak power of laser. In specifying system parameters, given in Fig. 7, the laser transmitter efficiency is assumed to be 0.9. The power returned to the device was calculated by assuming that the target was an ideal Lambertian surface with an albedo of 0.35. The lateral resolution is dictated by the diffraction limited spot size on the scene.

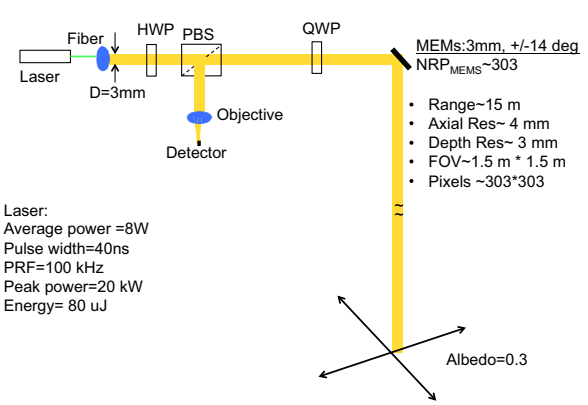

Fig. 7 LiDAR system. Not to scale.

The setup shown in Fig. 7 allows single element detectors to be used in a LiDAR system with subcentimeter range resolution. In parallel, we have developed 320×256 pixels

with 30-μm pixel pitch EI detector arrays, which are being integrated with the readout integrated circuits. Once realized, the EI imager can replace the single detector in the setup shown in Fig. 7 and improve performance specifications. Figure 7 gives a performance specification comparison based on our model between EI detector arrays with the detectors introduced in Sec. 5.[64]

5 Summary

SWIR photon detection has become an essential technology in the modern world. Sensitive SWIR detector arrays with high pixel density, low noise levels, and high SNRs are highly desirable for a variety of applications including biophotonics, LiDAR, optical tomography, and astronomical imaging. As such, many efforts in infrared detector research are directed toward improving the performance of the photon detectors operating in this wavelength range.

We review the history, principle of operation, present status, and application of a sensitive SWIR detector technology, which has demonstrated to be one of the most promising paths to high pixel density FPAs for low flux applications. The so-called EI detector was demonstrated for the first time in 2007. It offers an overall system-level sensitivity enhancement compared with the p-i-n diode due to a stable internal avalanche-free gain. The amplification method is inherently low noise, and devices exhibit an excess noise of unity. The detector operates in linear mode and requires only bias voltage of a few volts. The stable detector characteristics make formation of high yield, large-format and high pixel density FPAs less challenging compared with other detector technologies, such as avalanche photodetectors. The detector is based on the mature InP material system (InP/InAlAs/GaAsSb/InGaAs) and has a cutoff wavelength of 1700 nm.

EI detectors have been designed, fabricated, and tested during two generations of development and optimization cycles. The performance improvements in second-generation of devices have opened up many applications for these detectors in the medical field and remote sensing. We demonstrated the sensitivity advantage of using EI detectors in a time-of-flight LiDAR system. This was carried out through detailed theoretical models using experimentally measured device parameters. Using this model, we compared the performance of the EI detector, the commercial p-i-n detector, and the APD detector. The high internal gain, unity excess-noise, and excellent jitter of the EI detectors at room temperature allow the EI array to achieve good depth resolution and image quality. These also allow decreasing laser power and increasing receiver sensitivity while shrinking package size and power consumption.

Acknowledgments

V.F. and H.M. would like to acknowledge partial support from the National Science Foundation (NSF) Award No. IIP-1500314, Defense Advanced Research Projects Agency (DARPA)/Army Research Office (ARO) Award Nos. W911NF-11-1-0390, W911NF-12-1-0324, and W911NF-13-1-0485, as well as computational resources and staff contributions provided by the Quest high-performance computing facility at Northwestern University, which is jointly supported by the Office of the Provost, the Office for Research, and Northwestern University Information Technology. V. F. would also like to acknowledge the Ryan Fellowship support from Northwestern University.

References

1. C. Cohen-Tannoudji, J. Dupont-Roc, and G. Grynberg, *Photons and Atoms: Introduction to Quantum Electrodynamics*, Wiley-Interscience, New York (1997).
2. M. D. Eisaman et al., "Invited review article: single-photon sources and detectors," *Rev. Sci. Instrum.* **82**, 071101 (2011).
3. G. Lewis, "The conservation of photons," *Nature* **118**, 874–875 (1926).
4. "The cloud chamber," 1912, Wilson, http://www-outreach.phy.cam.ac.uk/camphy/cloudchamber/cloudchamber13_1.htm (27 February 2017).
5. N. Wermes, "Pixel detectors for particle physics and imaging applications," *Nucl. Instrum. Methods Phys. Res. A* **512**, 277–288 (2003).
6. "The physics of particle detectors," http://www.desy.de/~garutti/LECTURES/ParticleDetectorSS12/L1_Introduction_HEPdetectors.pdf (27 February 2017).
7. G. B. Heim, J. Burkepile, and W. W. Frame, "Low-light-level EMCCD color camera," *Proc. SPIE* **6209**, 62090F (2006).
8. E. Charbon, "Single-photon imaging in complementary metal oxide semiconductor processes," *Philos. Trans. Ser. A Math. Phys. Eng. Sci.* **2014**, 372 (2012).
9. C. G. Coates et al., "Backilluminated electron multiplying technology: the world's most sensitive CCD for ultralow-light microscopy," *Proc. SPIE* **4962**, 319–328 (2003).
10. A. J. P. Theuwissen, *Solid-State Imaging with Charge-Coupled Devices*, Kluwer Academic, Dordrecht (1996).
11. V. Fathipour, S. J. Jang, and H. Mohseni, "New generation of isolated electron-injection imagers," in *13th Workshop on Information Optics (WIO'14)*, Neuchatel, pp. 1–3 (2014).
12. H. Spieler, *Semiconductor Detector Systems*, Vol. **12**, Oxford University Press, England, U.K. (2005).
13. A. Pfenning et al., "Nanothermometer based on resonant tunneling diodes: from cryogenic to room temperatures," *ACS Nano* **9**, 6271–6277 (2015).
14. N. Wermes and G. Hallewel, "Technical design report of the ATLAS pixel detector," CERN/LHCC/98-13 (1998).
15. W. Erdmann, "The CMS pixel detector," *Nucl. Instrum. Methods Phys. Res. A* **447**, 178–183 (2000).
16. CMS, "The tracker system project," ALICE Collaboration, Technical Design Report, CERN/LHCC/98-006 (1998).
17. "ALICE technical design report," CERN/LHCC 99–12 (1999).
18. T. Gys, "The pixel hybrid photon detectors for the LHCb-RICH project," *Nucl. Instrum. Methods Phys. Res. A* **465**, 240–246 (2001).
19. P. Seitz and A. J. P. Theuwissen, *Single-Photon Imaging*, Springer Series in Optical Sciences, USA, Vol. **160** (2011).
20. S. S. Eikenberry, G. G. Fazio, and S. M. Ransom, "An SSPM-based high-speed near-infrared photometer for astronomy," *Publ. Astron. Soc. Pac.* **108**, 939 (1996).
21. A. Rogalski, "History of infrared detectors," *Opto–Electron. Rev.* **20**(3), 279–308 (2012).
22. A. Pfenning et al., "Photocurrent-voltage relation of resonant tunneling diode photodetectors," *Appl. Phys. Lett.* **107**, 081104 (2015).
23. J. Hynecek, "Impactron—a new solid state image intensifier," *IEEE Trans. Electron Devices* **48**, 2238–2241 (2001).
24. P. Jerram et al., "The LLLCCD: low light imaging without the need for an intensifier," *Proc. SPIE* **4306**, 178–186 (2001).
25. M. S. Robbins and B. J. Hadwen, "The noise performance of electron multiplying charge-coupled devices," *IEEE Trans. Electron Devices* **50**, 1227–1232 (2003).
26. J. Hynecek and T. Nishiwaki, "Excess noise and other important characteristics of low light level imaging using charge multiplying CCDs," *IEEE Trans. Electron Devices* **50**, 239–245 (2003).
27. "Concepts in digital imaging technology electron multiplying charge-coupled devices (EMCCDs)," http://hamamatsu.magnet.fsu.edu/articles/emccds.html (27 February 2017).
28. S. Ohta et al., "Characterization results of 1 k × 1 k charge-multiplying CCD image sensor," *Proc. SPIE* **5301**, 99–108 (2004).
29. M. S. Robbins, "The noise performance of electron multiplying charge-coupled devices," *IEEE Trans. Electron Devices* **50**(5), 1227–1232 (2003).
30. A. Goetzberger et al., "Avalanche effects in silicon p-n junctions. II. Structurally perfect junctions," *J. Appl. Phys.* **34**(6), 1591–1600 (1963).
31. K. Johnson, "High-speed photodiode signal enhancement at avalanche breakdown voltage," *IEEE Trans. Electron Devices* **12**(2), 55–63 (1965).
32. M. A. Itzler et al., "Comparison of 32 × 128 and 32 × 32 Geiger-mode APD FPAs for single photon 3D LADAR imaging," *Proc. SPIE* **8033**, 80330G (2011).
33. W. R. Clark et al., "A 1 cm × 1 cm In 0.53 Ga 0.47 As-In 0.52 Al 0.48 As avalanche photodiode array," *IEEE Photonics Technol. Lett.* **18**, 19–21 (2006).
34. E. de Borniol et al., "HgCdTe-based APD focal plane array for 2D and 3D active imaging: first results on a 320 × 256 with 30 $\hat{A}\mu$m pitch demonstrator," *Proc. SPIE* **7660**, 76603D (2010).
35. J. Rothman et al., "High operating temperature SWIR HgCdTe APDs for remote sensing," *Proc. SPIE* **9254**, 92540P (2014).
36. G. Finger et al., "Evolution of IR detection and possible outcomes for astrophysics," *EAS Publ. Ser.* **37**, 343–353 (2009).

37. Y. Bai et al., "Teledyne imaging sensors: silicon CMOS imaging technologies for x-ray, UV, visible, and near infrared," *Proc. SPIE* **7021**, 702102 (2008).
38. V. Fathipour, A. Bonakdar, and H. Mohseni, "Advances on sensitive electron-injection based cameras for low-flux, short-wave infrared applications," *Front. Mater.* **3**, 33 (2016).
39. P. Feautrier, J. Gach, and P. Wizinowich, "State of the art IR cameras for wavefront sensing using e-APD MCT arrays," in *First Light Imaging SAS*, First Light Imaging SAS, France (2015).
40. R. J. McIntyre, "Multiplication noise in uniform avalanche diodes," *IEEE Trans. Electron Devices* **ED-13**, 164–168 (1966).
41. K. Lau et al., "Excess noise measurement in avalanche photodiodes using a transimpedance amplifier front-end," *Meas. Sci. Technol.* **17**, 1941–1946 (2006).
42. M. A. Saleh et al., "Impact-ionization and noise characteristics of thin III-V avalanche photodiodes," *IEEE Trans. Electron Devices* **48**(12), 2722–2731 (2000).
43. M. M. Hayat et al., "Boundary effects on multiplication noise in thin heterostructure avalanche photodiodes: theory and experiment [Al0.6Ga0.4As/GaAs]," *IEEE Trans. Electron Devices* **49**(12), 2114–2123 (2002).
44. O.-H. Kwon et al., "Optimal excess noise reduction in thin heterojunction Al0.6Ga0.4As-GaAs avalanche photodiodes," *IEEE J. Quantum Electron.* **39**(10), 1287–1296 (2003).
45. G. Leveque et al., "Ionization energies in CdxHg1-xTe avalanche photodiodes," *Semicond. Sci. Technol.* **8**, 1317–1323 (1993).
46. V. F. Guelleca et al., "Linear photon-counting with HgCdTe APDs," *Proc. SPIE* **8375**, 83750Y (2012).
47. http://www.first-light.fr/wp-content/uploads/2015/07/Datasheet-C-RED_10.12.15.pdf
48. A. Rogalski, "Recent progress in infrared detector technologies," *Infrared Phys. Technol.* **54**, 136–154 (2011).
49. A. Rogalski, "Progress in focal plane array technologies," *Prog. Quantum Electron.* **36**, 342–473 (2012).
50. J. Gach and P. Feautrier, "Advances in imaging: Electron-initiated APDs improve high-speed SWIR imaging," *Laser Focus World* **51**(9), (2015).
51. N. K. Dhar, A. K. Sood, and R. Dat, *Advances in Infrared Detector Array Technology*, INTECH Open Access Publisher, Croatia (2013).
52. O. G. Memis et al., "A photon detector with very high gain at low bias and at room temperature," *Appl. Phys. Lett.* **91**, 171112 (2007).
53. V. Fathipour, S. J. Jang, and H. Mohseni, "New generation of isolated electron-injection imagers," in *IEEE 13th Workshop on Information Optics (WIO)*, Neuchatel, Switzerland (2014).
54. V. Fathipour et al., "Isolated electron injection detectors with high gain and record low dark current at telecom wavelength," *IEEE J. Sel. Top. Quantum Electron.* **20**, 65–70 (2014).
55. V. Fathipour and H. Mohseni, *CLEO—Laser Science to Photonic Applications*, OSA, San Jose (2015).
56. V. Fathipour et al., "Highly sensitive and linear electron-injection detectors at the telecomm wavelength," in *Frontiers in Optics 2014, OSA Technical Digest (online)*, Optical Society of America, Paper No. FW2A.4 (2014).
57. O. G. Memis et al., "Sub-Poissonian shot noise of a high internal gain injection photon detector," *Opt. Express* **16**(17), 12701 (2008).
58. Y. Movassaghi et al., "Analytical modeling and numerical simulation of the short-wave infrared electron-injection detectors," *Appl. Phys. Lett.* **108**, 121102 (2016).
59. V. Fathipour et al., "On the sensitivity of electron-injection detectors at low light level," *IEEE Photonics J.* **8**(3), 6803207 (2016).
60. O. G. Memis et al., "Signal-to-noise performance of a short-wave infrared nanoinjection imager," *Opt. Lett.* **35**(16), 2699 (2010).
61. O. G. Memis et al., "A short-wave infrared nano-injection imager with 2,500 A/W responsivity and low excess noise," *IEEE Photonics J.* **2**, 858–864 (2010).
62. V. Fathipour et al., "Impact of three-dimensional geometry on the performance of isolated electron-injection infrared detectors," *Appl. Phys. Lett.* **106**(2), 021116 (2015).
63. V. Fathipour and H. Mohseni, "A new detector for high-speed swept source optical coherence tomography," *Proc. SPIE* **9609**, 96090A (2015).
64. V. Fathipour et al., "Modeling of a sensitive time of flight flash Lidar," *Proc. SPIE* **9974**, 99740N (2016).
65. T. Ahmed et al., "Optical quilt packaging: a new chip-to-chip optical coupling and alignment process for modular sensors," in *CLEO: 2014, OSA Technical Digest (online)*, Optical Society of America, Paper No. JTu4A.56 (2014).
66. T. Ahmed et al., "Label free detection of phospholipids by infrared absorption spectroscopy," *Proc. SPIE* **9166**, 91660H (2014).
67. R. Moss et al., "Low-cost compact MEMS scanning ladar system for robotic applications," *Proc. SPIE* **8379**, 837903 (2012).
68. S. D. Mayor and S. M. Spuler, "Raman-shifted eye-safe aerosol lidar," *Appl. Opt.* **43**, 3915–3924 (2004).
69. P. Yuan et al., "32 × 32 Geiger-mode ladar camera," *Proc. SPIE* **7684**, 76840C (2010).
70. E. De Borniol et al., "A 320 × 256 HgCdTe avalanche photodiode focal plane array for passive and active 2D and 3D imaging," *Proc. SPIE* **8012**, 801232 (2011).
71. A. Poloczek et al., "Integrated InGaAs pin-diode on exactly oriented silicon (001) substrate suitable for 10 Gbit/s digital applications," in *The 20th Annual Meeting of the IEEE Lasers and Electro-Optics Society (LEOS)*, pp. 180–181 (2007).
72. B. L. Stann et al., "Brassboard development of a MEMS-scanned ladar sensor for small ground robots," *Proc. SPIE* **8037**, 80371G (2011).
73. M. Stipčević, H. Skenderović, and D. Gracin, "Characterization of a novel avalanche photodiode for single photon detection in VIS-NIR range," *Opt. Express* **18**, 17448–17459 (2010).
74. Y. Liang et al., "Low-timing-jitter single-photon detection using 1-GHz sinusoidally gated InGaAs/InP avalanche photodiode," *IEEE Photonics Technol. Lett.* **23**(13), 887–889 (2011).
75. M. A. Itzler et al., "Single photon avalanche diodes (SPADs) for 1.5 μm photon counting applications," *J. Mod. Opt.* **54**(2), 283–304 (2007).
76. R. Heinrichs et al., "Three-dimensional laser radar with APD arrays," *Proc. SPIE* **4377**, 106–117 (2001).
77. N. K. Dhar, R. Dat, and A. K. Sood, "Advances in infrared detector array technology," in *Optoelectronics–Advanced Materials and Devices*, S. Pyshkin, Ed., InTech Open Access Publisher (2013).
78. V. Fathipour et al., "Approaching high temperature photon counting with electron-injection detectors," *Proc. SPIE* **9220**, 92200J (2014).
79. "Semiconductoor electronic properties," http://www.ioffe.ru/SVA/NSM/Semicond/GaInAs/highfield.html (27 February 2017).

Vala Fathipour is a postdoctoral scholar at the University of California-Berkeley working on the development of state-of-the-art LiDAR systems. She received her PhD in electrical engineering, solid-state and photonics from Northwestern University. Her research interests include design, fabrication, and characterization of single-photon infrared detectors, optical coherence tomography, and light detection and ranging system development. She has published 30 conference papers and 11 peer-reviewed articles.

Hooman Mohseni is a professor of electrical engineering and computer sciences at Northwestern University. He is the recipient of several research and teaching awards, including the NSF CAREER Award, DARPA Young Faculty Award, and Northwestern Faculty Honor Roll. He serves on the editorial boards of *IEEE Photonics*, *IEEE Selected Topics in Quantum Electronics*, *Optics Letter*, and *Frontiers in Material*. He has published over 120 peer-reviewed articles in major journals, including *Nature*, *Nano Letters*, and *ACS Nano*. He holds 14 issued US and international patents. He is a fellow of SPIE and OSA.